Nanoscale
Advances

ROYAL SOCIETY
OF CHEMISTRY

PAPER

View Article Online
View Journal | View Issue

Open Access Article. Published on 25 August 2021. Downloaded on 2/22/2026 9:18:43 AM.
This article is licensed under a Creative Commons Attribution-NonCommercial 3.0 Unported Licence.

Check for updates

Cite this: *Nanoscale Adv.*, 2021, **3**, 6074

Role of Ce concentration on the structural and magnetic properties of functional magnetic oxide particles

Jyoti Saini,[a] Monika Sharma[ab] and Bijoy Kumar Kuanr *[a]

Received 25th March 2021
Accepted 25th August 2021

DOI: 10.1039/d1na00227a

rsc.li/nanoscale-advances

Functional magnetic oxide particles offer exceptional GHz frequency capabilities, which can significantly enhance the utility of communication and signal processing devices. In the present work, we have investigated the structural and magnetic properties of rational multifunctional oxide $Y_{2.9-x}Ce_xBi_{0.1}Fe_5O_{12}$ particles – a full series with $x = 0.0$, 0.2, 0.4, 0.6, 0.8 and 1 *via* a conventional solid-state route. The X-ray diffraction pattern validated the $Ia\bar{3}d$ cubic garnet phase in all samples. From Rietveld refinement, it is observed that the ceric oxide (CeO_2) impurity increases with an increase of Ce concentration, evincing a partial substitution of cerium (Ce) element into the garnet structure. The magnetic oxide particles with Ce concentration $x = 0.4$ showed a better crystallite size, dodecahedral site occupancy and solubility of cerium in the garnet phase. The morphological visualization of random shaped grains in the micrometer range was performed using the scanning electron microscopy (SEM) technique. The static magnetic properties showed that the saturation magnetization (M_s) decreases up to 43% and coercivity increases up to 59% with the increase of Ce concentration. The dynamic investigation on these oxide particles exhibits various intriguing and novel properties. Various intrinsic material parameters such as saturation magnetization (M_s), gyromagnetic ratio (γ), Gilbert damping constant (α) and extrinsic contribution (ΔH_o) to linewidth were determined from the fitting of resonance field (H_r) and field linewidth (ΔH_r) data. We ascertained that the damping constant increases with the increase of Ce concentration, which can be explained in terms of two magnon scattering and local defects caused by CeO_2 inhomogeneity. The proposed doped garnets can be a potential candidate for high frequency microwave applications and spin-transfer-torque devices.

I. Introduction

Multiferroics is a well known subject of next generation multifunctional materials, which amalgamates simultaneously magnetic, electric and elastic properties.[1–10] Multifunctional materials have attracted a lot of interest due to their fascinating electric, magnetic and optical properties.[11–20] This has led to a variety of technological applications such as microwave devices, spintronics, sensors, transducers, energy harvesting, random access multi-state memories, data storage recording technologies and communication systems.[21–41] Since the last three to four decades, yttrium iron oxide (YIG) has been established as one of the promising multifunctional materials due to its potential electromagnetic properties such as high saturation magnetization, low damping constant (order of 10^{-5}), longer spin-wave propagation length, high resistivity ($\sim 10^{13}$ Ω cm), moderate thermal expansion coefficient, low ohmic losses and high Faraday rotation, which are very important for magnetic, spintronic, magnonic and high frequency microwave devices.[42–53]

In recent years, doping of rare earth (RE) and transition metals in YIG has attracted tremendous interest due to their modified magnetic, optical and electrical properties suitable for new applications such as 5G telecommunication and drug delivery systems.[54–60] The performance of rare earth substituted garnets (RE:YIG) relies upon the dopant type, amount of dopant and preparation technique.[61–65] Specifically, the study of bismuth and cerium substituted YIG has attracted a lot of interest due to their high Faraday rotation and strong magneto-optical activity at near infrared telecommunication wavelengths.[52,53,56,65] Cerium (Ce) element has amazing quality as it can be effortlessly exchangeable between the 4+ valence state and 3+ valence state.[66] Also, cerium substituted yttrium iron oxide has attracted much attention due to its remarkable multiferroic (MF) properties such as magneto-dielectric (MD) and strong magneto-optical (MO) effects.[67–69] Soumah Lucile, *et al.* demonstrated that bismuth substituted yttrium iron oxide (Bi:YIG) leads to extremely low Gilbert damping together with perpendicular magnetic anisotropy (PMA).[70] Goto Taichi, *et al.* reported that enhanced

---

[a] *Special Centre for Nanoscience, Jawaharlal Nehru University, New Delhi, 110067, India. E-mail: bkkuanr@gmail.com*

[b] *Department of Physics, Deshbandhu College, University of Delhi, New Delhi, 110019, India*

© 2021 The Author(s). Published by the Royal Society of Chemistry

Open Access Article. Published on 25 August 2021. Downloaded on 2/22/2026 9:18:43 AM.
This article is licensed under a Creative Commons Attribution-NonCommercial 3.0 Unported Licence.

magneto-optical properties with very low optical losses can be accomplished with the cerium substitution in YIG.[71] Higuchi and the co-workers have achieved Ce:YIG thin films for magnetic sensor application.[72] Fu Chen *et al.* reported the enhanced magneto-dielectric response with increase of cerium content.[69] A. Ikesue *et al.* showed that the Faraday rotation increases from 144 deg. cm^{-1} for 1 at% of Ce to 990 deg. cm^{-1} for 8 at% of Ce substitution in YIG.[73] They also reported that Faraday rotation for Ce doped garnet was around 5 times higher than that of 1 at% of Bi substitution. Elhamali *et al.* investigated the influence of erbium (Er) on the structural, magnetic and optical properties of Ce:YIG films.[74] M. R. Khalifeh reported recently the effect of Dy^{3+} incorporation on the structural and magnetic properties of $Y_{2.8-x}Dy_xCe_{0.1}Bi_{0.1}Fe_5O_{12}$ garnet.[75] In spite of the fact that cerium strongly manipulates the magnetic, dielectric, thermal and optical properties of YIG,[67–69,71–73] its solubility inside the garnet phase is still a challenging task.

The only magnetic ion in yttrium iron oxide (YIG) is Fe^{3+}. In each molecular formula unit, Y^{3+} ions occupy dodecahedral sites surrounded with eight oxygen ions, namely the "c" site, whereas three out of five Fe^{3+} ions occupy the tetrahedral "d" site surrounded with four oxygen ions and the rest of the two Fe^{3+} ions are present at the octahedral "a" site surrounded with six oxygen ions. The controlling super-exchange interaction renders the magnetic moments of the "a" and "d" site positions antiparallel.[76]

In the present investigation, engineered and custom-modified garnet based multifunctional oxides having the representative formula $Y_{2.9-x}Ce_xBi_{0.1}Fe_5O_{12}$ (or $Ce_xBi_{0.1}$:YIG with $x = 0.0, 0.2, 0.4, 0.6, 0.8$ and 1) have been synthesized by a conventional solid-state reaction method. We systematically investigated the phase identification with crystal structure analysis and cerium solubility inside the garnet structure. Also, we studied elemental analysis, morphological/microstructural analysis, and static and dynamic magnetic properties. Mao Tze-Chern, *et al.* reported the maximum solubility of cerium in YIG for 2% cerium content.[77] However, in the present investigation we successfully observed that the solubility of cerium element in the garnet phase can be achievable up to 4% cerium concentration and decreases with a further increase. It is also confirmed by the maximum value of dodecahedral site occupancy for the $x = 0.4$ sample. The magnetic squareness increases with Ce increment. From the ferromagnetic resonance (FMR) measurements we have observed the magnetic damping constant to increase with Ce-content. It has to be mentioned here that the increased damping ameliorate for spin-transfer-torque devices.

II. Experimental details

The investigated garnet based oxides were synthesized by the conventional solid state reaction method from the oxide powders of Y_2O_3 (yttrium(III) oxide), Bi_2O_3 (bismuth(III) oxide), CeO_2 (cerium(IV) oxide), and Fe_2O_3 (iron(III) oxide) from Sigma Aldrich with purity >99%. The fine oxide powders were mixed at a stoichiometric proportion with an accuracy of 1 mg and mixed well by grinding in a pestle-mortar with the addition of ethanol for 12 hours at room temperature. This synthesis method is advantageous as it is cost-effective, reduces pollution, requires less synthesis steps, simple in handling and gives a homogeneous product for commercial purpose. The benefit of using this method is to obtain a large particle size so that the number of grain boundaries and corresponding losses can be minimized.[78] After that, the completely dried mixture was annealed at 1250 °C for 10 hours under an air atmosphere.[79] Thereafter, uniform pellets were formed with 0.3 g of sintered oxide powders and 5 wt% polyvinyl alcohol (PVA) aqueous solution as a binder under 450 MPa pressure. The size of the obtained pellets was about 10 mm in diameter and 1 mm in thickness. Pressed pellets were sintered at 1350 °C for 6 hours under an air atmosphere.[79] Fig. 1 shows the schematic representation of the synthesis process. The studied samples with compositions $Y_{2.9-x}Ce_xBi_{0.1}Fe_5O_{12}$ ($x = 0.0, 0.2, 0.4, 0.6, 0.8$ and 1) were labelled as S1, S2, S3, S4, S5 and S6 respectively.

The X-ray diffraction (XRD) technique was used to examine the phases and crystal structure of the synthesized samples. Room temperature XRD analysis of powdered samples was carried out with a Miniflex 600 X-ray diffractometer from Rigaku with an X-ray radiation source CuKα ($\lambda = 1.54181$ Å) at 40 kV and 15 mA in the diffraction angle (2θ) range of 20°–80°, with a step size of 0.02° and a scanning speed of 5° min^{-1}. All the observed XRD profiles were fitted with the pseudo-Voigt peak profile function using Rietveld analysis on FullProf Suite software. The Raman spectra were recorded using an Enspectr Raman spectrometer in the range 150–800 cm^{-1} using a green laser source with a power of 300 mW and a wavelength of 532 nm. The rigorous analysis of Raman spectra has been performed using the Gaussian peak profile function for multiple peak fitting. Scanning electron microscopy (SEM) (ZEISS EVO40 electron microscope) was used to visualize the surface morphology and analyze the grain size distribution of gold

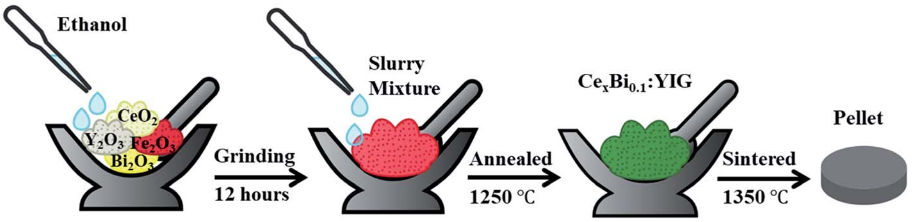

Fig. 1 Schematic representation of $Y_{2.9-x}Ce_xBi_{0.1}Fe_5O_{12}$ magnetic oxides.

Open Access Article. Published on 25 August 2021. Downloaded on 2/22/2026 9:18:43 AM.
This article is licensed under a Creative Commons Attribution-NonCommercial 3.0 Unported Licence.

coated sintered pellets. The grain size statistical distribution was obtained from Gaussian fitting of histograms (for approximately 150 grains) showing different grain sizes present in the respective samples. In order to analyze more accurately the grain size distribution, the histogram has been plotted with three to four SEM images of each sample. EDX measurements were also used to identify the desired proportion of elemental compositions. High resolution transmission electron microscopy (HRTEM) was performed at 200 kV using a JEOL 2100F transmission electron microscope (TEM) and sample preparation was done by drop-casting the ethanol dispersed powdered samples on carbon grid mesh. Room temperature magnetic hysteresis loops of the powder samples were measured using VSM (Cryogenics, UK.) by the application of DC magnetic field up to 10 kOe. The coercivity (H_c) was calculated precisely from the M–H curve. Moreover, the saturation magnetization (M_s) and first order magneto-crystalline anisotropy constant K_1 were calculated from linear fitting of the law of approach to saturation or LAS (*i.e.* M *vs.* $1/H^2$ plot) using saturated data points of the first quadrant of the M–H loop. Room temperature dynamic magnetic properties of the studied samples have been studied using the conventional ferromagnetic resonance (FMR) technique in field sweep mode using a flip-chip geometry. FMR is a magnificent dynamic technique to study the microwave absorption (MA) properties of the magnetic materials.[54,80,81] A vector network analyzer (VNA) was used to generate microwave energy, whereas a coplanar waveguide (CPW) was used as a device for propagation of EM-waves. The samples were placed on a CPW in flip-chip geometry. In this technique, microwave energy interacts with the magnetic oxide samples before being dissipated as heat to the lattice. In the FMR technique, the external magnetic field leads to the precession of magnetic moments in the ferromagnetic material and was applied at right angle to the radio frequency (RF) magnetic field of the signal line which satisfies the FMR condition. In the field sweep mode, frequency (f) was kept fixed, whereas external DC magnetic field was swept from 0 to 12 kOe range in a step of 20 Oe. The measurements were performed for a broad range of frequencies from 6 GHz to 22 GHz. The S_{21} parameters (scattering matrix transmission parameters) were recorded for each DC magnetic field using computer controlled software. The S_{21} data show a resonance dip at FMR and the precise resonance field (H_r) and field linewidth (ΔH_r) were obtained from Lorentzian fitting to the FMR data. Also, the various intrinsic and extrinsic contributions to field and linewidth were determined from the fitting of resonance field (H_r) and field linewidth (ΔH_r) plots.

III. Results and discussion

A. XRD results

Fig. 2(a) shows the powdered XRD patterns of the investigated multifunctional magnetic oxides. The XRD pattern confirms the formation of $Ia\bar{3}d$ cubic symmetry of the yttrium iron oxide (YIG) phase (JCPDS data no. 43-0507). Also, additional secondary phase of CeO_2 (JCPDS card no. 81-0792) is observed in doped YIG samples as denoted by the symbol *. The existence of CeO_2 impurities reveals the partial substitution of cerium element into the garnet structure.[77] Rietveld refinement of the crystal structure from the experimental XRD profile is performed in a two phase model using FullProf Suite software and the goodness of fit parameter (χ^2) is refined to the acceptable limit. The refinement of XRD data is performed by minimizing the difference between observed and calculated diffraction peaks of substituted YIG samples. The crystal structure is drawn using VESTA software after refinement of XRD profiles as shown in Fig. 2 (b–e). Also, the experimental and refined diffraction patterns of all the oxide samples are shown in Fig. 3(a–f). All the refined parameters using FullProf Suite software are tabulated in Tables 1–4. It is observed from the results (Table 1) that the lattice constant depends upon ionic radii of doped elements (*i.e.* Ce^{3+} and Bi^{3+}). Also, lattice constant is inversely related to the dodecahedral site occupancy and directly related to the ionic radii. From the refined results, we observed that the density increases with Ce-content in

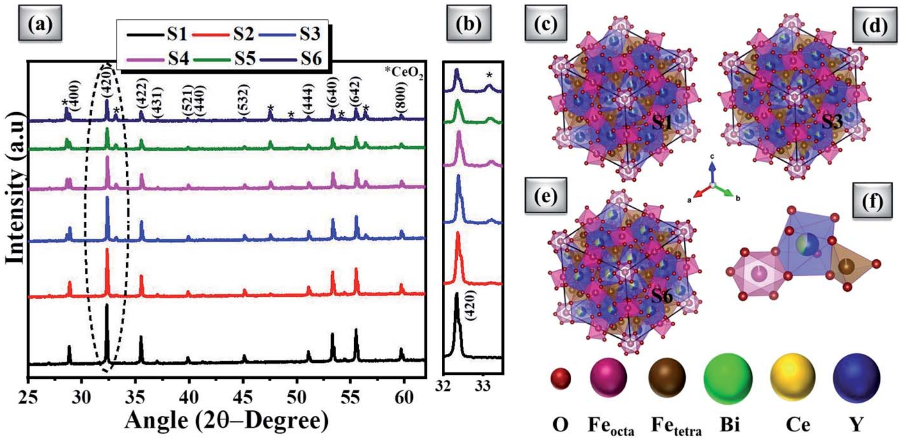

Fig. 2 (a) Room temperature XRD patterns, and (b) zoom out of the most intense peak. (c–e) Show the refined crystal structure of $Ce_xBi_{0.1}$:YIG where $x = 0.0$ (S1), 0.4 (S3) and 1.0 (S6) respectively. (f) shows all three polyhedrons present in the garnet structure *i.e.* Y^{3+} ion attached with eight oxygen in the dodecahedral site, three Fe^{3+} attached with four oxygen (Fe_{tetra}) in the tetrahedral site and rest of the two Fe^{3+} attached with six oxygen (Fe_{octa}) in the octahedral site respectively.

© 2021 The Author(s). Published by the Royal Society of Chemistry

Open Access Article. Published on 25 August 2021. Downloaded on 2/22/2026 9:18:43 AM.
This article is licensed under a Creative Commons Attribution-NonCommercial 3.0 Unported Licence.

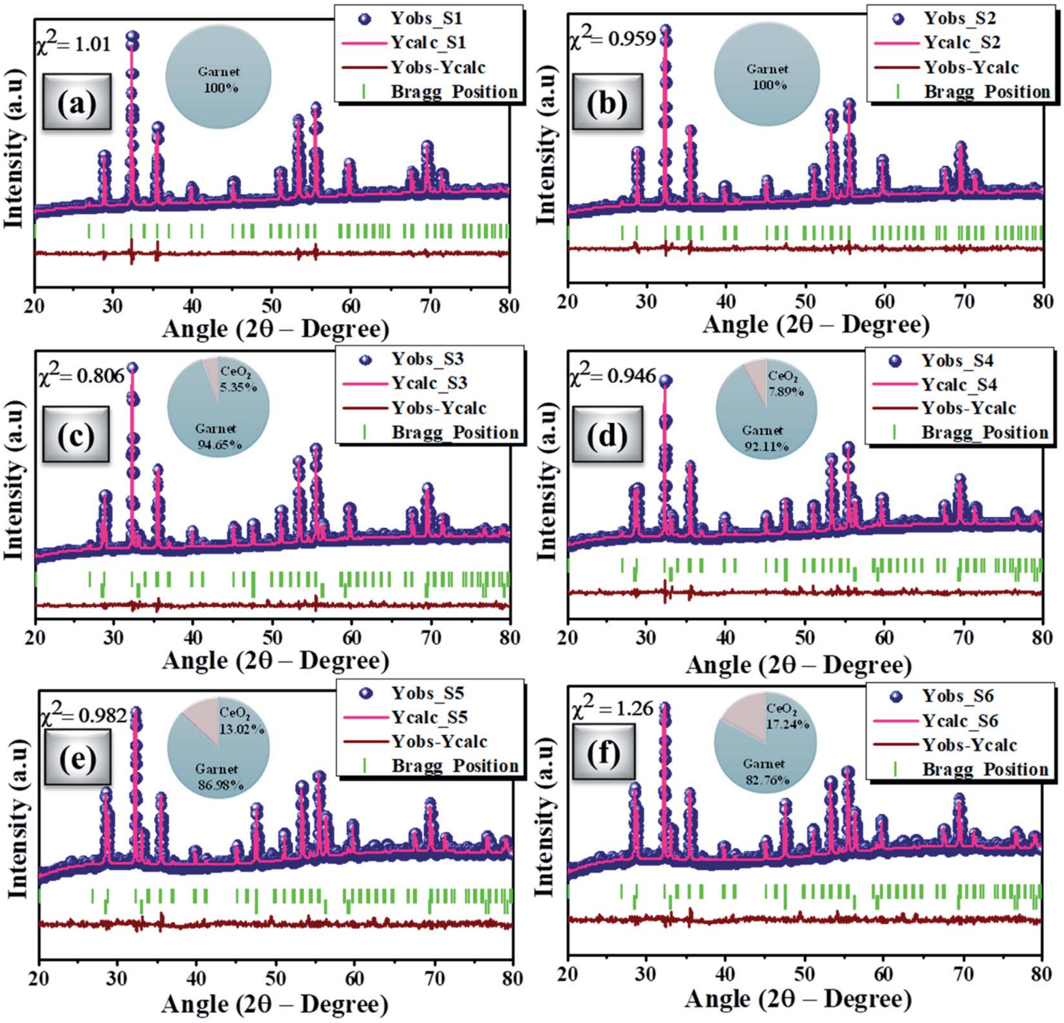

Fig. 3 (a–f) The Rietveld refinement of $Ce_xBi_{0.1}$:YIG magnetic oxides using FullProf Suite software.

Table 1 Refined XRD parameters at room temperature (300 K)

Sample name	Lattice constant (Å)	Volume (Å^3)	X-ray density (g cm^{-3})
S1	12.3835	1899.03	4.988 ± 0.01
S2	12.3945	1904.07	4.999 ± 0.01
S3	12.3918	1902.87	5.244 ± 0.01
S4	12.3924	1903.12	5.199 ± 0.01
S5	12.3929	1903.33	5.255 ± 0.01
S6	12.3884	1901.29	5.415 ± 0.01

investigated oxide samples. Further, the value of dodecahedral site occupancy (Table 2) is found to be maximum for the $x = 0.4$ sample which interprets the better solubility of cerium element in the garnet phase and decreases further. The improvement of cerium solubility in the garnet structure is better as compared to previous reports.[77] Table 3 presents the refined bond lengths of R–O*, R–O** (R–Y, Bi, and Ce), $Fe^{(T)}$–O and $Fe^{(O)}$–O in all the samples. In yttrium iron oxide, the Y^{3+} ion is bonded to the Fe^{3+} ion by oxygen, resulting in a creation of two different length R–O* and R–O** bonds. Consequently, two different angles are formed for each Fe^{3+} ion located in the tetrahedral and octahedral sublattices corresponding to two oxygen bond lengths.[82–84]

Fig. 4(a) shows the average crystallite size (D) and lattice strain (ε) of doped magnetic oxides which are calculated using the size–strain plot (SSP) from eqn (1);[85]

$$(d \times \beta \times \cos\theta)^2 = \left(\frac{\kappa\lambda}{D}\right) \times (d^2 \times \beta \times \cos\theta) + \left(\frac{\varepsilon}{2}\right)^2 \quad (1)$$

Table 2 Refined site occupancy

	Site occupancy (R = Y, Bi, Ce)			
Sample name	O	R	$Fe^{(T)}$	$Fe^{(O)}$
S1	1	0.924	0.908	0.965
S2	1	0.909	0.904	0.967
S3	1	0.948	0.962	0.991
S4	1	0.910	0.935	0.983
S5	1	0.896	0.933	0.977
S6	1	0.931	0.973	0.973

Open Access Article. Published on 25 August 2021. Downloaded on 2/22/2026 9:18:43 AM.
This article is licensed under a Creative Commons Attribution-NonCommercial 3.0 Unported Licence.

Table 3 Refined bond length

	Bond length (Å) (R = Y, Bi, Ce)			
Sample name	R–O*	R–O**	$Fe^{(T)}$–O	$Fe^{(O)}$–O
S1	2.38353	2.39364	1.9083	2.00031
S2	2.35747	2.41445	1.88898	2.02289
S3	2.36407	2.42665	1.87094	2.02619
S4	2.40746	2.40195	1.9074	1.98647
S5	2.35796	2.44368	1.84448	2.04432
S6	2.34886	2.42924	1.87056	2.03048

Here, d is the interplanar spacing which is calculated using Bragg's law ($2d \sin \theta = n\lambda$), β is the full-width at half-maximum (FWHM), θ is the Bragg angle, κ is the shape factor (~0.9), and λ is the X-ray wavelength (Cu Kα ~1.54181 Å). The results showed that with the increase of Ce concentration in $Ce_xBi_{0.1}$:YIG magnetic oxides, the lattice strain increases up to $x = 0.4$ Ce concentration. The positive sign of lattice strain signifies the tensile nature, which is perhaps due to larger ionic radii of Ce^{3+} and Bi^{3+} ions as compared to the Y^{3+} ion [*i.e.* Y^{3+} (1.02 Å), Ce^{3+} (1.14 Å) and Bi^{3+} (1.17 Å)].[86] The crystallite size in all the samples is in accordance with the value of strain. Fig. 4(b) shows the variation of lattice constant and dodecahedral site occupancy with cerium concentration and Fig. 4(c) shows the behaviour of crystallite size and strain with cerium concentration. The calculated values of crystallite size and lattice strain from the size–strain plot are tabulated in Table 5.[85] One of the major findings from the XRD confirms that cerium element solubility increases inside the garnet structure up to $x = 0.4$ at. wt%.

B. Raman spectroscopy

Fig. 5(a) shows the Raman spectra of magnetic oxide pellets. According to the group theory, the cubic symmetry of the garnet based crystal structure represents 25 Raman modes ($3\ A_{1g} + 8\ E_g + 14\ F_{2g}$).[87,88] The Raman spectra of the doped YIG pellet

Table 4 Refined bond angle

	Bond angle (deg.) (R = Y, Bi, Ce)					
Sample name	R–O–R	$Fe^{(T)}$–O– $Fe^{(O)}$	R–O*–$Fe^{(T)}$	R–O**–$Fe^{(T)}$	R–O*–$Fe^{(O)}$	R–O**–$Fe^{(O)}$
S1	105.066	124.623	91.648	123.224	103.946	103.588
S2	105.357	124.616	93.061	123.272	104.276	102.295
S3	104.737	125.390	93.293	123.465	103.907	101.751
S4	104.175	125.621	91.025	122.995	103.642	103.838
S5	104.405	125.856	94.199	123.876	103.554	100.658
S6	105.083	125.102	93.757	123.287	104.263	101.495

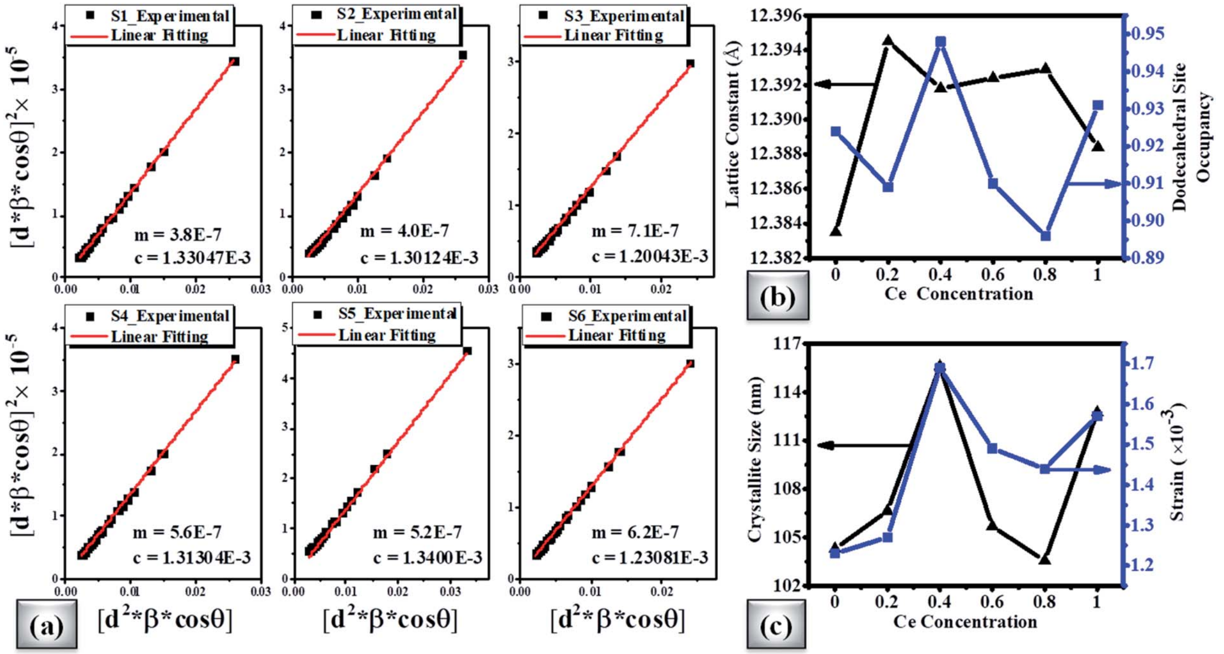

Fig. 4 (a) The size–strain plots for average crystallite size 'D' and lattice strain 'ε' of all the complex oxide samples. (b) The variation of lattice constant and dodecahedral site occupancy for different cerium (Ce) concentrations. (c) The variation of average crystallite size 'D' and strain 'ε' with Ce concentration.

© 2021 The Author(s). Published by the Royal Society of Chemistry

Open Access Article. Published on 25 August 2021. Downloaded on 2/22/2026 9:18:43 AM.
This article is licensed under a Creative Commons Attribution-NonCommercial 3.0 Unported Licence.

Table 5 The strain size plot (SSP) results

Sample name	D (nm)	Strain × 10^{-3}	Adj. $\mathbb{R}^2$
S1	104.29	1.23	0.999
S2	106.64	1.27	0.996
S3	115.59	1.69	0.999
S4	105.68	1.49	0.999
S5	103.55	1.44	0.993
S6	112.74	1.57	0.999

demonstrate peaks around 154, 168, 190, 235, 269, 338, 368, 415, 441, 502, 580, 675, 700, and 727 cm^{-1} respectively. The ferrimagnetic nature can be linked with the most intense peak at 269 cm^{-1}. The partial substitution of Ce element in the garnet phase can be depicted by CeO_2 degenerated vibrational mode near 462 cm^{-1} for higher Ce-content samples. The Raman spectra of $Ce_xBi_{0.1}$:YIG ($x = 0.0$, 0.2, 0.4, 0.6, 0.8 and 1.0) garnets clearly show peak shifting due to induced lattice strain. It is observed that the Raman shift of the most intense T mode (or translational mode) around 269 cm^{-1} depends upon the Fe$^{(T)}$–O bond length of doped YIG crystal as shown in Fig. 5(b).[54] In addition, the full width at half maximum (FWHM) can be directly related to the doping at the dodecahedral site as shown in Fig. 5(c). The intensity variation of T + T_1 + T_2 and T modes present at 190, 235 and 269 cm^{-1} with Ce concentration is presented in Fig. 5(d), where T_1, T_2 and T translation refer to Fe_{octa}^{3+}, R^{3+} and $[Fe_{tetra}O_4]^{5-}$ respectively. These results confirmed good crystalline nature for $x = 0.4$ Ce concentration and generation of lattice strain due to cerium doping.

C. Microstructural/morphological study

Morphological visualization and statistics of grain size distribution were studied by scanning electron microscopy (SEM). The SEM images of investigated samples S1, S3 and S6 are presented in Fig. 6(a–c). The SEM snapshots unveiled the random shaped grains. The grain size distribution study has been performed using Gaussian fitting of histograms as shown in the inset of Fig. 6(a–c). Digimizer software was used to analyse the grain size distribution. From Gaussian fitting, the average grain size is observed in the micrometer range and that is comparatively bigger than that from previous studies.[75,89–91] It is clear from the SEM micrographs that, for higher cerium concentration the primary particle order gets densified along with lattice diffusion which can be correlated with the ionic radii of the doped elements (*i.e.* Ce^{3+} and Bi^{3+}).[92] As observed that the density increases with Ce concentration there are chances of grain boundary diffusion causing enhanced grain size. SEM images reveal that the grain size increases from 5 μm to 12 μm for samples S1 to S6. Also, the agglomeration increases

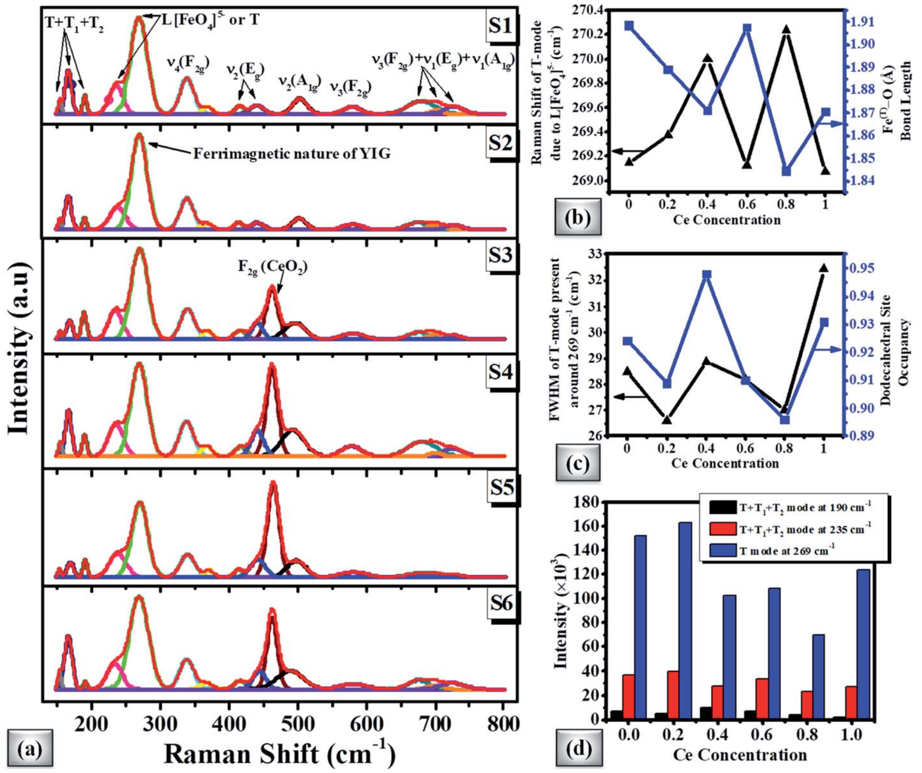

Fig. 5 (a) Raman spectra of the investigated oxide samples; here, different colour curves represent the individual peak fitting with Gaussian profile function where the red colour curve represents the cumulative fitting of Raman spectra. (b) The variation of Raman Shift of T-mode at 269 cm^{-1} and Fe$^{(T)}$–O bond length at different cerium (Ce) concentrations. (c) The variation of FWHM of T-mode at 269 cm^{-1} and dodecahedral site occupancy for various Ce concentrations in doped YIG samples. (d) Histogram showing intensity variation of Raman modes present at 190 cm^{-1}, 235 cm^{-1} and 269 cm^{-1} as a function of Ce concentration.

Open Access Article. Published on 25 August 2021. Downloaded on 2/22/2026 9:18:43 AM.
This article is licensed under a Creative Commons Attribution-NonCommercial 3.0 Unported Licence.

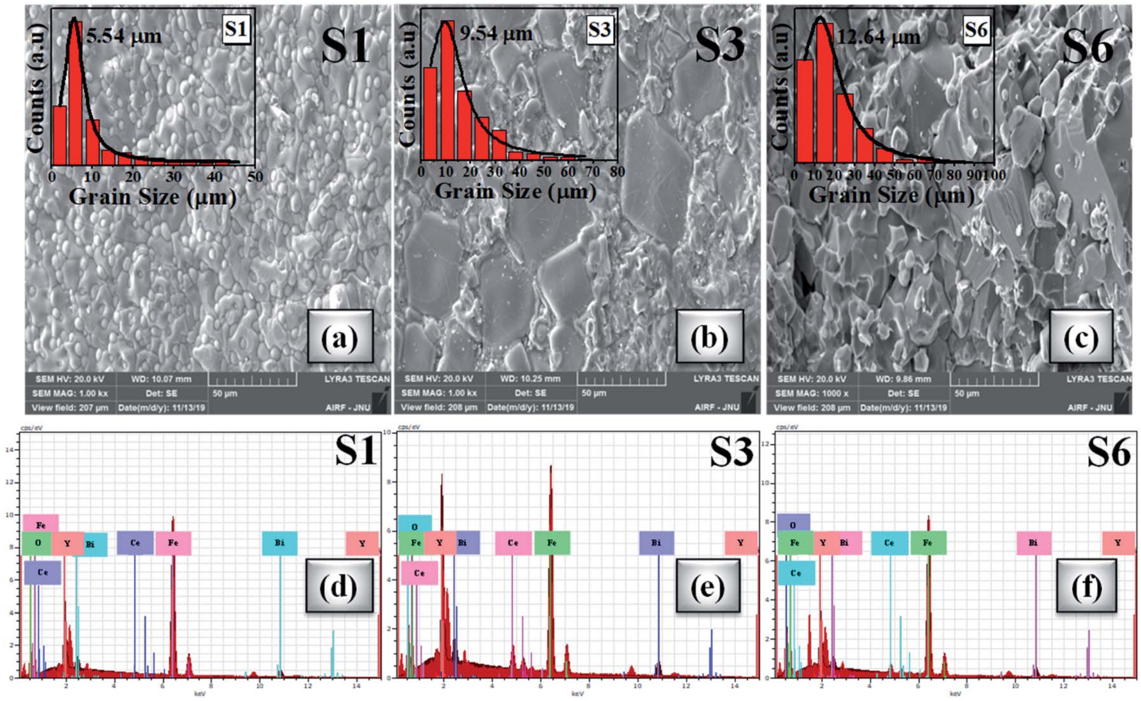

Fig. 6 (a–c) SEM micrographs of S1, S3 and S6 oxide samples (inset: Gaussian distribution of grain sizes). (d–f) EDX spectra of S1, S3 and S6 samples.

because of different compositions and their presence may depend upon magnetic interaction and the chemical reaction during the sintering process at a particular temperature which shows better alignment between the grains.[92] Fig. 6(d–f) shows the EDX analysis which discloses the presence of elemental compositions. We interpreted from the morphological analysis that the oxide particles show a large grain size for the $x = 0.4$ Ce sample like a monocrystalline phase.

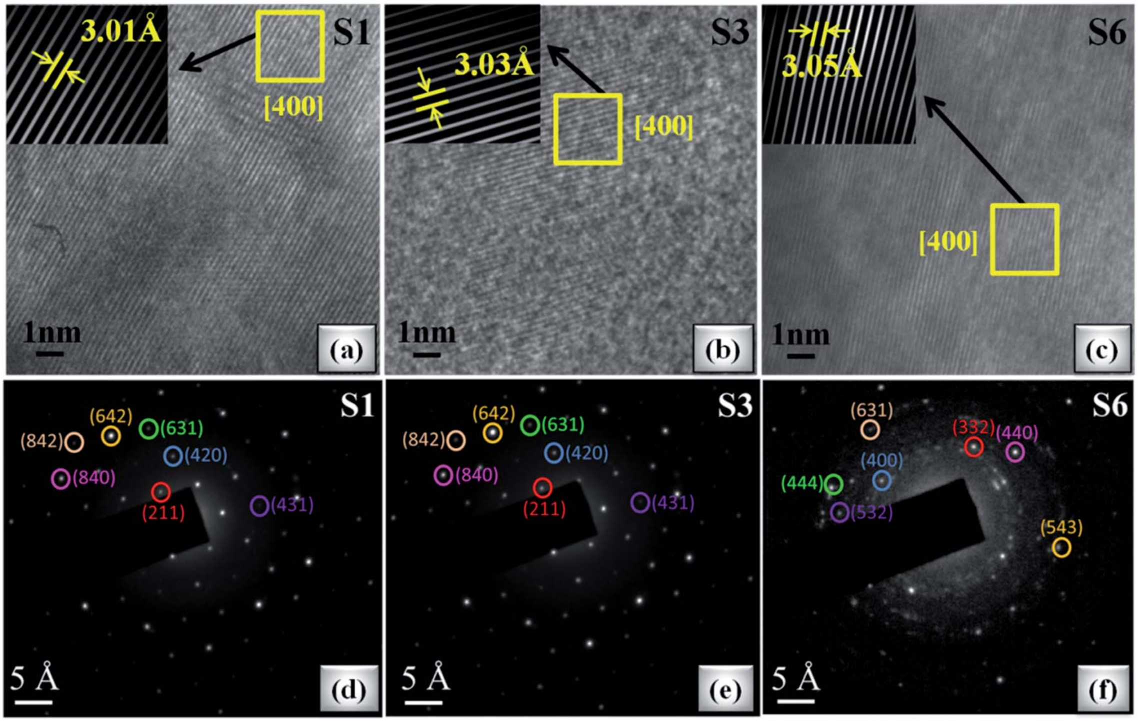

Fig. 7 (a–c) HRTEM images of S1, S3 and S6 oxide samples (inset: inverse FFT of the selected region). (d–f) SAED pattern of S1, S3 and S6 samples.

Open Access Article. Published on 25 August 2021. Downloaded on 2/22/2026 9:18:43 AM. This article is licensed under a Creative Commons Attribution-NonCommercial 3.0 Unported Licence.

Fig. 7(a–c) shows the HRTEM images of S1, S3 and S6 samples. It can be seen that samples S1 and S3 show clear fringes, which reflects good crystallinity, and for sample S6, blurred fringes are observed on account of accentuated ceric oxide impurity. The *d*-spacing of HRTEM micrographs is calculated by inverse finite Fourier transform (FFT) method and is in accordance with the planes indexed in the XRD pattern. The maximum portion in each HRTEM image corresponds to the (400) crystal plane, confirming the mono-crystalline behaviour which is also confirmed by the SAED pattern as shown in Fig. 7(d–f). The SAED patterns are indexed by calculating *d*-values using the distance between the central spot and investigated spot. The calculated *d*-values of the SAED pattern are very well matched with the *d*-values calculated using Bragg's law and support most of the planes indexed in the XRD pattern. It is observed from the SAED pattern that S1 and S3 show good monocrystalline nature of studied garnet structures. With a further increase of Ce concentration (>S3 sample), due to the increase of CeO_2, distortion increases, resulting in polycrystalline nature as shown in Fig. 7(f).

D. Static and dynamic magnetization study

Static magnetic properties. Fig. 8(a) shows the room temperature magnetic hysteresis loop (*M–H* curve) of the studied magnetic oxide powders. It is clear that all the samples show soft magnetic nature. The saturation magnetization and magneto crystalline anisotropy are determined from the LAS method using eqn (2).[54]

$$M = M_S\left[1 - \frac{8{K_1}^2}{105{\mu_0}^2{M_s}^2H^2}\right] - \chi H \tag{2}$$

where M is the magnetization, M_s is the saturation magnetization, K_1 is the first order anisotropy constant, μ_0 is the free space permeability, H is the applied magnetic field and χH is the paramagnetic part. Fig. 8(b) shows the M *vs.* $1/H^2$ plot formed with saturated data points of the first quadrant of the M–H loop. It is observed that the saturation magnetization (M_s) decreases from 26.316 emu g^{-1} to 14.999 emu g^{-1} with the increase of Ce concentration. The behaviour of saturation magnetization can be explained by Neel's theory,[93,94] which claims that super-exchange interaction renders the magnetic moments of "a" and "d" sites in antiparallel positions. Here, Fe^{3+} sublattices are antiferromagnetically coupled to the R^{3+} (*i.e.* Y^{3+}, Ce^{3+} and Bi^{3+}) sublattices.[93–96] As a result, the net magnetic moment can be written as eqn (3);

$$\begin{aligned}\mathrm{M_{net}} = |M(3\mathrm{Fe_{tetra}}^{3+}) - M(2\mathrm{Fe_{octa}}^{3+})| - M(\mathrm{RE}^{3+}) = \\ M(\mathrm{Fe_{tetra}}^{3+}) - M(\mathrm{RE}^{3+})\end{aligned} \tag{3}$$

The M_s decreases in view of the fact that Ce^{3+} paramagnetic ions have a magnetic moment of 1 μ_B and there is no contribution either from Y^{3+} or Bi^{3+} diamagnetic ions (each having

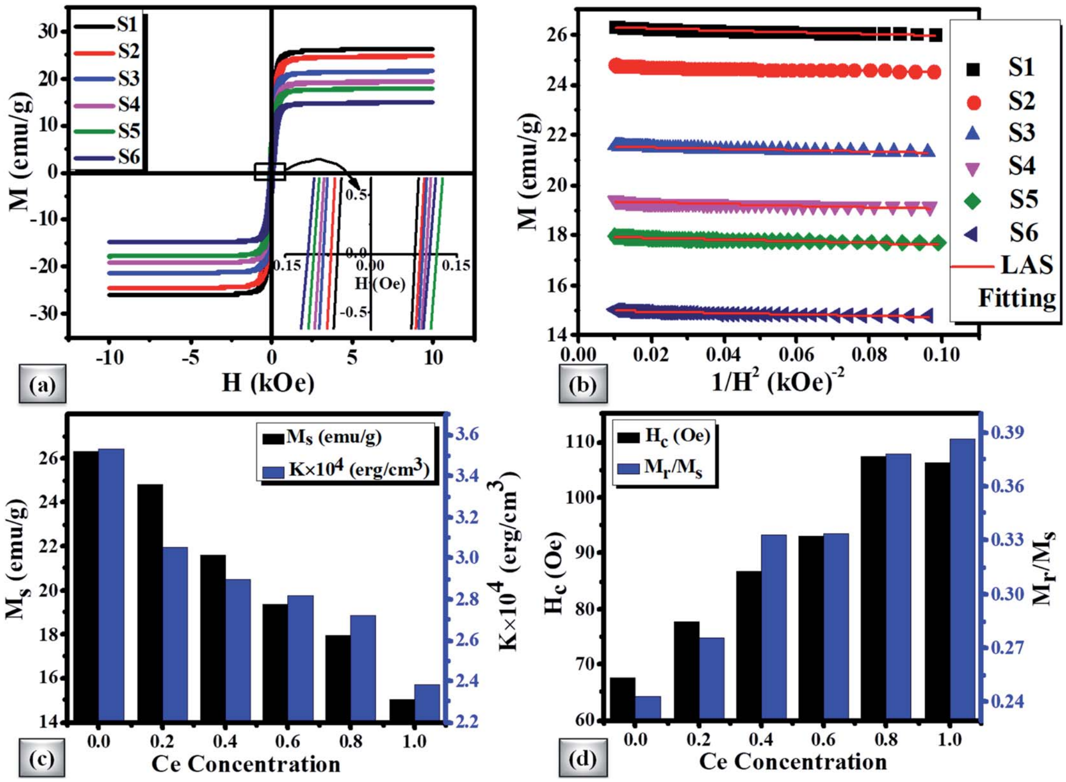

Fig. 8 (a) The room temperature magnetic hysteresis loop of $Ce_xBi_{0.1}$:YIG magnetic oxides. (b) LAS plot. (c) The variation of saturation magnetization (M_s) and first order anisotropy constant K_1 at different Ce concentrations. (d) The variation of coercive field and magnetic squareness with Ce-content.

Open Access Article. Published on 25 August 2021. Downloaded on 2/22/2026 9:18:43 AM.
This article is licensed under a Creative Commons Attribution-NonCommercial 3.0 Unported Licence.

a magnetic moment of 0 μ_B).[97] The saturation magnetization also decreases with the increase of non-magnetic CeO_2 phase which results in oxygen reduction leading to the conversion of Fe^{3+} ions to Fe^{2+} ions. The variation of saturation magnetization (M_S) and first order magneto-crystalline anisotropy constant K_1 at different Ce concentrations is shown in Fig. 8(c). The magneto-crystalline anisotropy results from the interaction of the electron orbitals with the potentials of the lattice. So, it is directly affected by lattice distortion due to the increase of Ce content.[98] It is observed that the coercive force (H_c) increases up to 59% with the increase of Ce-content which may be attributed to lattice strain and ceric oxide inhomogeneity.

The magnetic squareness (M_r/M_s) is also showing similar behaviour with a Ce content from 0.243 to 0.386 respectively. This increase in squareness can be related to the transformation of the magnetic oxide phase to monocrystalline nature and inclined orientation towards the magnetic easy axis. The variation of H_c and M_r/M_s with Ce-content is demonstrated in Fig. 8(d). The observed magnetic parameters are tabulated in Table 6.

Dynamic magnetic parameters. Standard ferromagnetic resonance (FMR) spectroscopy is a well-established technique to explore the dynamic magnetic properties of ferromagnetic materials. In this technique, interaction between the ferromagnetic material and microwave energy is measured before the energy is dissipated in the form of heat. Field sweep broadband FMR measurements of all the samples are performed in flip-chip geometry on a CPW. The scattering parameters (S_{21}) are measured from the VNA. The external magnetic field is applied in order to satisfy the FMR condition.[54] The FMR spectra of sample S1 as a function of externally applied biasing field for various frequencies in a 3D colour map surface with projection are shown in Fig. 9(a).

From the FMR spectra, we determined the resonance field (H_r) and field linewidth (ΔH) as a function of frequency for all

Table 6 Room temperature magnetic parameters from VSM and FMR

	Static magnetic parameters				Dynamic magnetic parameters				
Sample	M_s (emu g^{-1})	H_c (Oe)	M_r/M_s	$K_1 \times 10^4$ (erg cm^{-3})	M_s (kOe)	γ' (GHz kOe^{-1})	H_{ani} (kOe)	ΔH_o (Oe)	α
S1	26.316	67.656	0.243	3.53	1.648	2.78	0.191	378	1.3×10^{-3}
S2	24.783	77.631	0.275	3.05	1.556	2.86	0.187	450	1.4×10^{-3}
S3	21.570	86.657	0.332	2.90	1.42	2.9	0.186	535	1.9×10^{-3}
S4	19.355	92.946	0.333	2.82	1.263	2.93	0.224	615	2.0×10^{-3}
S5	17.940	107.346	0.378	2.72	1.184	2.97	0.229	668	2.5×10^{-3}
S6	14.999	106.392	0.386	2.38	1.02	2.86	0.231	562	1.9×10^{-3}

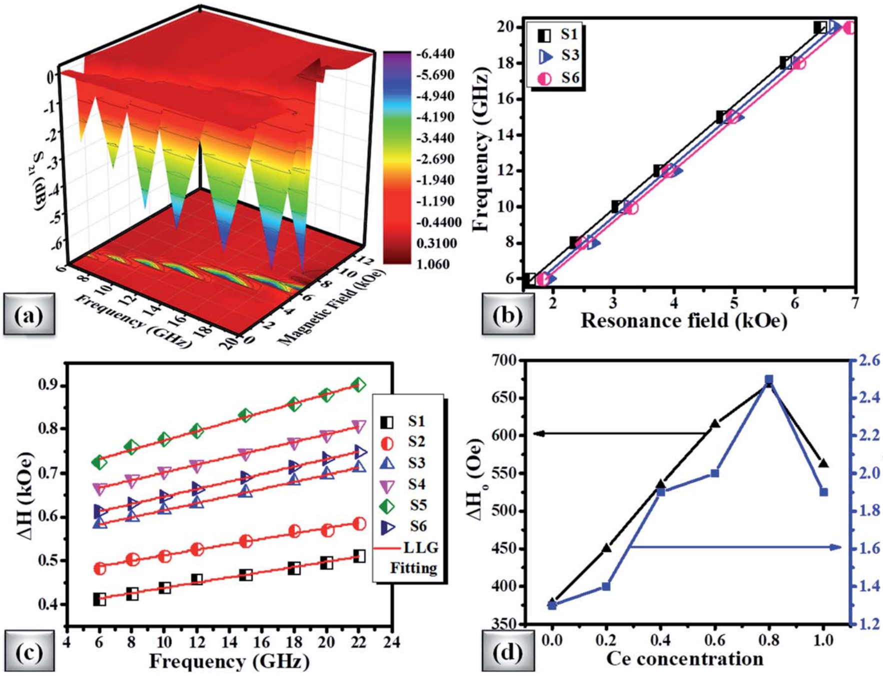

Fig. 9 (a) The field sweep 3D colour map surface with projection of microwave absorption at various frequencies of the S1 sample. (b) The applied operating frequency (*f*) as a function of resonance field (H_r) for S1, S3, and S6 samples. (c) The FMR linewidth (ΔH) *versus* applied operating frequency (*f*) for all the investigated samples. (d) Intrinsic (α) and extrinsic contribution (ΔH_O) of linewidth as a function of Ce concentration.

© 2021 The Author(s). Published by the Royal Society of Chemistry

Open Access Article. Published on 25 August 2021. Downloaded on 2/22/2026 9:18:43 AM.
This article is licensed under a Creative Commons Attribution-NonCommercial 3.0 Unported Licence.

Table 7 Comparison with other literature works

Parameters	$Bi_{0.1}$:YIG[104–106]	Ce_x:YIG[54,77,92,107,108]	$Ce_xBi_{0.1}$:YIG (present work)
Cerium solubility	—	0.2 at. wt%	0.4 at. wt%
Crystallite size (nm)	65	93	104–115
Grain size (μm)	—	0.3	5.5–12.6
M_s (emu g^{-1})	21.81	25.12–20	26.32–15.0
H_c (Oe)	17.72	12	67.66–107.35
M_r/M_s	0.063	0.0–0.05	0.24–0.39
α	2.0×10^{-3}	2.8×10^{-3}	1.3×10^{-3}

the samples using Lorentzian fitting. Fig. 9(b) shows the operational frequency as a function of resonance field for samples S1, S3 and S6 respectively. For spherical nanoparticles, we can use the Kittel expression as given in eqn (4) for determining the intrinsic material parameters;[99,100]

$$f = \gamma'(H_r + H_{eff}) \tag{4}$$

$$H_{eff} = H_D + H_{ani} + H_{int} \tag{5}$$

Here, f is the microwave frequency, $\gamma = 2\pi\gamma' = g\mu_B/\hbar$ is the gyromagnetic ratio, H_r is the ferromagnetic resonance field, H_{eff} is the effective field and it is a combination of many fields represented by eqn (5), where $H_D = -(4\pi M_S)/3$ is the demagnetizing field for spherical nanoparticles, H_{ani} is the anisotropy field and H_{int} represents the internal field which is negligible for soft magnetic materials. The saturation magnetization, gyromagnetic ratio (γ) and anisotropy field of the multifunctional oxide samples were obtained from the fitting of eqn (4) and their values are tabulated in Table 6.

The derived FMR linewidth (ΔH) is a combination of the intrinsic and extrinsic contribution. The intrinsic contribution arises due to material properties and extrinsic contribution is due to defects and inhomogeneous broadening. It is observed that ΔH increases with the increase of Ce-content up to sample S5 and further addition decreases ΔH for sample S6. This can be explained as the lattice distortion and dodecahedral site occupancy increase up to S5 (as shown in Fig. 4(b)) and decrease further for sample S6. Fig. 9(c) shows the FMR linewidth (ΔH) as a function of applied operating frequency (f) for all the magnetic oxide samples. The observed data were fitted to a line by considering the Landau–Lifshitz–Gilbert (LLG) model represented by eqn (6);[101,102]

$$\Delta H = \Delta H_0 + \frac{2\alpha f}{\gamma'} \tag{6}$$

where α is the Gilbert damping constant known as the intrinsic damping parameter. ΔH_0 is the frequency independent ($f = 0$) contribution to ΔH produced by inhomogeneous broadening also called as extrinsic contribution to linewidth. Extrinsic contribution can be explained by a two-magnon scattering mechanism.[103] Two magnon scattering results when uniform mode magnons are scattered into degenerate spin wave states with wave vector $k \neq 0$. This scattering is caused by the presence of magnetic inhomogeneities such as defects and non-uniformity. ΔH_0 is extracted from the intercept and α from the slope by the fitting to LLG eqn (6). It is seen that the Gilbert damping constant and ΔH_0 increase with the increase of Ce-content which may be ascribed to two magnon scattering and ceric oxide inhomogeneity.[103]

The deteriorating values of ΔH_0 and α for $x = 1.0$ cerium concentration can be decoded by the increase in dodecahedral site occupancy value as shown in Fig. 4(b). The studied properties of the present investigation have been compared with other literature works in Table 7.

From the ensemble of Table 7, we like to emphasize that the observed parameters like cerium solubility, crystallite size, grain size, saturation magnetization, coercivity, squareness ratio and magnetic damping are better than the earlier reported data. Hence, the present investigated series, especially $x = 0.4$ cerium concentration composition, can be a good candidate for spin-transfer torque MRAM (STT-MRAM) devices and magnetic sensor applications.

IV. Conclusion

Succinctly, a meticulous study for the fabrication of doped magnetic oxides has been successfully carried out using a solid state reaction method. The detailed analysis of the phase and crystal structure was performed using Rietveld refinement of XRD data. We demonstrated that with the increase of Ce concentration lattice distortion increases due to lattice strain and CeO_2 impurities. SSP results showed the tensile nature of strain together with large crystallite sizes (>100 nm). The SEM micrographs asserted the existence of very large grain size in the micrometer range (5–12 μm). Saturation magnetization decreased up to 43% due to Ce^{3+} paramagnetic ions and coercivity increased up to 59%. The generation of strain-induced anisotropy was clearly evident from the dc magnetic measurements, whereas the magnetization dynamic study clearly showed that the microwave absorption decreases with the increase of Ce content. It was also observed that the Gilbert damping parameter (α) and extrinsic contribution (ΔH_0) increase with Ce concentration. In conclusion, we demonstrated that the cerium substitution maneuvers the saturation magnetization, anisotropy field and Gilbert damping together with large crystallite and grain sizes. Such observed properties will be good for new generation microwave devices, spin-transfer-torque devices such as spin-transfer torque MRAM

© 2021 The Author(s). Published by the Royal Society of Chemistry

Open Access Article. Published on 25 August 2021. Downloaded on 2/22/2026 9:18:43 AM.
This article is licensed under a Creative Commons Attribution-NonCommercial 3.0 Unported Licence.

(STT-MRAM), and magnetic sensors with multi-functional features.

Conflicts of interest

There are no conflicts to declare.

Acknowledgements

This work was supported by the MHRD-IMPRINT grant, DST-SERB, DST-AMT grant of Govt. of India. One of the authors (Jyoti Saini) is thankful to the Ministry of Human Resource Development, Govt. of India, for providing Prime Minister's Research Fellowship.

References

1 J. Wu, Z. Fan, D. Xiao, J. Zhu and J. Wang, Multiferroic bismuth ferrite-based materials for multifunctional applications: ceramic bulks, thin films and nanostructures, *Prog. Mater. Sci.*, 2016, **84**, 335–402.
2 M. Bibes and A. Barthélémy, Towards a magnetoelectric memory, *Nat. Mater.*, 2008, **7**(6), 425–426.
3 C. A. Vaz, J. Hoffman, C. H. Ahn and R. Ramesh, Magnetoelectric coupling effects in multiferroic complex oxide composite structures, *Adv. Mater.*, 2010, **22**(26–27), 2900–2918.
4 M. M. Vopson, Fundamentals of multiferroic materials and their possible applications, *Crit. Rev. Solid State Mater. Sci.*, 2015, **40**(4), 223–250.
5 N. Ortega, A. Kumar, J. F. Scott and R. S. Katiyar, Multifunctional magnetoelectric materials for device applications, *J. Phys.: Condens. Matter*, 2015, **27**(50), 504002.
6 K. Ramam, B. S. Diwakar, K. Varaprasad, V. Swaminadham and V. Reddy, Magnetic properties of nano-multiferroic materials, *J. Magn. Magn. Mater.*, 2017, **442**, 453–459.
7 G. S. Lotey and N. K. Verma, Multiferroic properties of Tb-doped BiFeO 3 nanowires, *J. Nanopart. Res.*, 2013, **15**(4), 1–14.
8 S. Ravi and C. Senthilkumar, Multiferroism in new Bi_2FeMoO_6 material, *Mater. Express*, 2015, **5**(1), 68–72.
9 R. Liu, Y. Zhao, R. Huang, Y. Zhao and H. Zhou, Multiferroic ferrite/perovskite oxide core/shell nanostructures, *J. Mater. Chem.*, 2010, **20**(47), 10665–10670.
10 C. Lu, W. Hu, Y. Tian and T. Wu, Multiferroic oxide thin films and heterostructures, *Appl. Phys. Rev.*, 2015, **2**(2), 021304.
11 G. Subramanyam, M. W. Cole, N. X. Sun, T. S. Kalkur, N. M. Sbrockey, G. S. Tompa, X. Guo, C. Chen, S. P. Alpay, G. A. Rossetti Jr and K. Dayal, Challenges and opportunities for multi-functional oxide thin films for voltage tunable radio frequency/microwave components, *J. Appl. Phys.*, 2013, **114**(19), 13.
12 C. Wang, H. Xu, C. Liang, Y. Liu, Z. Li, G. Yang, L. Cheng, Y. Li and Z. Liu, Iron oxide@polypyrrole nanoparticles as a multifunctional drug carrier for remotely controlled cancer therapy with synergistic antitumor effect, *ACS Nano*, 2013, **7**(8), 6782–6795.
13 S. H. Baek and C. B. Eom, Epitaxial integration of perovskite-based multifunctional oxides on silicon, *Acta Mater.*, 2013, **61**(8), 2734–2750.
14 N. Izyumskaya, Y. Alivov and H. Morkoc, Oxides, oxides, and more oxides: high-κ oxides, ferroelectrics, ferromagnetics, and multiferroics, *Crit. Rev. Solid State Mater. Sci.*, 2009, **34**(3–4), 89–179.
15 Tsymbal, E. Y., Dagotto, E. R., Eom, C. B. and Ramesh, R., *Multifunctional Oxide Heterostructures*, Oxford University Press, 2012.
16 Y. Xue, H. Chen, D. Yu, S. Wang, M. Yardeni, Q. Dai, M. Guo, Y. Liu, F. Lu, J. Qu and L. Dai, Oxidizing metal ions with graphene oxide: the *in situ* formation of magnetic nanoparticles on self-reduced graphene sheets for multifunctional applications, *Chem. Commun.*, 2011, **47**(42), 11689–11691.
17 K. J. Jin, H. B. Lu, K. Zhao, C. Ge, M. He and G. Z. Yang, Novel multifunctional properties induced by interface effects in perovskite oxide heterostructures, *Adv. Mater.*, 2009, **21**(45), 4636–4640.
18 X. Chen, Z. Tang, P. Liu, H. Gao, Y. Chang and G. Wang, Smart utilization of multifunctional metal oxides in phase change materials, *Matter*, 2020, **3**(3), 708–741.
19 Y. M. Huh, Y. W. Jun, H. T. Song, S. Kim, J. S. Choi, J. H. Lee, S. Yoon, K. S. Kim, J. S. Shin, J. S. Suh and J. Cheon, In vivo magnetic resonance detection of cancer by using multifunctional magnetic nanocrystals, *J. Am. Chem. Soc.*, 2005, **127**(35), 12387–12391.
20 S. R. Singamaneni, J. T. Prater and J. Narayan, Multifunctional epitaxial systems on silicon substrates, *Appl. Phys. Rev.*, 2016, **3**(3), 031301.
21 M. M. Vopson, Fundamentals of multiferroic materials and their possible applications, *Crit. Rev. Solid State Mater. Sci.*, 2015, **40**(4), 223–250.
22 M. Bibes and A. Barthelemy, Oxide spintronics, *IEEE Trans. Electron Devices*, 2007, **54**(5), 1003–1023.
23 J. Huang, H. Wang, X. Sun, X. Zhang and H. Wang, Multifunctional La0. $67Sr_{0.33}MnO_3$ (LSMO) thin films integrated on mica substrates toward flexible spintronics and electronics, *ACS Appl. Mater. Interfaces*, 2018, **10**(49), 42698–42705.
24 G. Pacchioni, Two-dimensional oxides: Multifunctional materials for advanced technologies, *Chem.–Eur. J.*, 2012, **18**(33), 10144–10158.
25 W. Chen, X. Hou, X. Shi and H. Pan, Two-dimensional Janus transition metal oxides and chalcogenides: multifunctional properties for photocatalysts, electronics, and energy conversion, *ACS Appl. Mater. Interfaces*, 2018, **10**(41), 35289–35295.
26 Pawade, V.B., Salame, P.H. and Bhanvase, B.A., *Multifunctional Nanostructured Metal Oxides for Energy Harvesting and Storage Devices*. CRC Press, 2020.
27 Guo, Z., Chen, Y. and Lu, N. L., *Multifunctional Nanocomposites for Energy and Environmental Applications*, John Wiley & Sons, 2018.

© 2021 The Author(s). Published by the Royal Society of Chemistry

Open Access Article. Published on 25 August 2021. Downloaded on 2/22/2026 9:18:43 AM.
This article is licensed under a Creative Commons Attribution-NonCommercial 3.0 Unported Licence.

28 G. Pacchioni, Two-dimensional oxides: Multifunctional materials for advanced technologies, *Chem.–Eur. J.*, 2012, **18**(33), 10144–10158.

29 F. A. Blyakhman, N. A. Buznikov, T. F. Sklyar, A. P. Safronov, E. V. Golubeva, A. V. Svalov, S. Y. Sokolov, G. Y. Melnikov, I. Orue and G. V. Kurlyandskaya, Mechanical, electrical and magnetic properties of ferrogels with embedded iron oxide nanoparticles obtained by laser target evaporation: Focus on multifunctional biosensor applications, *Sensors*, 2018, **18**(3), 872.

30 L. Zhang, W. F. Dong and H. B. Sun, Multifunctional superparamagnetic iron oxide nanoparticles: design, synthesis and biomedical photonic applications, *Nanoscale*, 2013, **5**(17), 7664–7684.

31 M. Opel, S. Geprägs, E. P. Menzel, A. Nielsen, D. Reisinger, K. W. Nielsen, A. Brandlmaier, F. D. Czeschka, M. Althammer, M. Weiler and S. T. Goennenwein, Novel multifunctional materials based on oxide thin films and artificial heteroepitaxial multilayers, *Phys. Status Solidi A*, 2011, **208**(2), 232–251.

32 G. Subramanyam, M. W. Cole, N. X. Sun, T. S. Kalkur, N. M. Sbrockey, G. S. Tompa, X. Guo, C. Chen, S. P. Alpay, G. A. Rossetti Jr. and K. Dayal, Challenges and opportunities for multi-functional oxide thin films for voltage tunable radio frequency/microwave components, *J. Appl. Phys.*, 2013, **114**(19), 191301.

33 H. Liu, Recent progress in atomic layer deposition of multifunctional oxides and two-dimensional transition metal dichalcogenides, *J. Mol. Eng. Mater.*, 2016, **4**(04), 1640010.

34 N. Izyumskaya, Y. Alivov and H. Morkoc, Oxides, oxides, and more oxides: high-κ oxides, ferroelectrics, ferromagnetics, and multiferroics, *Crit. Rev. Solid State Mater. Sci.*, 2009, **34**(3–4), 89–179.

35 H. Wang, X. Liang, J. Wang, S. Jiao and D. Xue, Multifunctional inorganic nanomaterials for energy applications, *Nanoscale*, 2020, **12**(1), 14–42.

36 M. Mohapatra and S. Anand, Synthesis and applications of nano-structured iron oxides/hydroxides–a review, *Int. J. Eng. Sci. Technol.*, 2010, **2**(8), 127–146.

37 K. Salonitis, J. Pandremenos, J. Paralikas and G. Chryssolouris, Multifunctional materials: engineering applications and processing challenges, *Int. J. Adv. Manuf. Technol.*, 2010, **49**(5–8), 803–826.

38 G. Subramanyam, M. W. Cole, N. X. Sun, T. S. Kalkur, N. M. Sbrockey, G. S. Tompa, X. Guo, C. Chen, S. P. Alpay, G. A. Rossetti Jr and K. Dayal, Challenges and opportunities for multi-functional oxide thin films for voltage tunable radio frequency/microwave components, *J. Appl. Phys.*, 2013, **114**(19), 13.

39 M. M. El-Hammadi and J. L. Arias, Iron oxide-based multifunctional nanoparticulate systems for biomedical applications: a patent review (2008–present), *Expert Opin. Ther. Pat.*, 2015, **25**(6), 691–709.

40 R. Hao, R. Xing, Z. Xu, Y. Hou, S. Gao and S. Sun, Synthesis, functionalization, and biomedical applications of multifunctional magnetic nanoparticles, *Adv. Mater.*, 2010, **22**(25), 2729–2742.

41 A. B. Ustinov, A. V. Drozdovskii and B. A. Kalinikos, Multifunctional nonlinear magnonic devices for microwave signal processing, *Appl. Phys. Lett.*, 2010, **96**(14), 142513.

42 L. Soumah, N. Beaulieu, L. Qassym, C. Carrétéro, E. Jacquet, R. Lebourgeois, J. B. Youssef, P. Bortolotti, V. Cros and A. Anane, Ultra-low damping insulating magnetic thin films get perpendicular, *Nat. Commun.*, 2018, **9**(1), 1–6.

43 M. Collet, O. Gladii, M. Evelt, V. Bessonov, L. Soumah, P. Bortolotti, S. O. Demokritov, Y. Henry, V. Cros, M. Bailleul and V. E. Demidov, Spin-wave propagation in ultra-thin YIG based waveguides, *Appl. Phys. Lett.*, 2017, **110**(9), 092408.

44 J. R. Eshbach, Spin-wave propagation and the magnetoelastic interaction in yttrium iron garnet, *J. Appl. Phys.*, 1963, **34**(4), 1298–1304.

45 G. P. Gauthier, A. Courtay and G. M. Rebeiz, Microstrip antennas on synthesized low dielectric-constant substrates, *IEEE Trans. Antennas Propag.*, 1997, **45**(8), 1310–1314.

46 Y. S. Chen, J. G. Lin, S. Y. Huang and C. L. Chien, Incoherent spin pumping from YIG single crystals, *Phys. Rev. B*, 2019, **99**(22), 220402.

47 D. C. Bullock and D. J. Epstein, Negative Resistance, Conductive Switching, and Memory Effect in Silicon-Doped Yttrium-Iron Garnet Crystals, *Appl. Phys. Lett.*, 1970, **17**(5), 199–201.

48 R. W. Cooper, W. A. Crossley, J. L. Page and R. F. Pearson, Faraday rotation in YIG and TbIG, *J. Appl. Phys.*, 1968, **39**(2), 565–567.

49 M. Wu and A. Hoffmann, *Recent Advances in Magnetic Insulators-From Spintronics to Microwave Applications*, 2013.

50 A. A. Serga, A. V. Chumak and B. Hillebrands, YIG magnonics, *J. Phys. D: Appl. Phys.*, 2010, **43**(26), 264002.

51 S. A. Nikitov, D. V. Kalyabin, I. V. Lisenkov, A. Slavin, Y. N. Barabanenkov, S. A. Osokin, A. V. Sadovnikov, E. N. Beginin, M. A. Morozova, Y. A. Filimonov and Y. V. Khivintsev, Magnonics: a new research area in spintronics and spin wave electronics, *Phys.-Usp.*, 2015, **58**(10), 1002.

52 M. Gomi, K. Satoh and M. Abe, Giant Faraday rotation of Ce-substituted YIG films epitaxially grown by RF sputtering, *Jpn. J. Appl. Phys.*, 1988, **27**(8A), L1536.

53 H. Uchida, Y. Masuda, R. Fujikawa, A. V. Baryshev and M. Inoue, Large enhancement of Faraday rotation by localized surface plasmon resonance in Au nanoparticles embedded in Bi:YIG film, *J. Magn. Magn. Mater.*, 2009, **321**(7), 843–845.

54 V. Sharma and B. K. Kuanr, Magnetic and crystallographic properties of rare-earth substituted yttrium-iron garnet, *J. Alloys Compd.*, 2018, **748**, 591–600.

55 M. Yousaf, A. Noor, S. Xu, M. N. Akhtar and B. Wang, Magnetic characteristics and optical band alignments of rare earth (Sm+ 3, Nd+ 3) doped garnet ferrite nanoparticles (NPs), *Ceram. Int.*, 2020, **46**(10), 16524–16532.

Open Access Article. Published on 25 August 2021. Downloaded on 2/22/2026 9:18:43 AM. This article is licensed under a Creative Commons Attribution-NonCommercial 3.0 Unported Licence.

56 M. Huang and S. Y. Zhang, Growth and characterization of cerium-substituted yttrium iron garnet single crystals for magneto-optical applications, *Appl. Phys. A: Solids Surf.*, 2002, **74**(2), 177–180.

57 J. F. Dillon Jr, Ferrimagnetic resonance in rare-earth-doped yttrium iron garnet. III. Linewidth, *Phys. Rev.*, 1962, **127**(5), 1495.

58 G. J. Chen and L. F. Wang, Design of magnetic nanoparticles-assisted drug delivery system, *Curr. Pharm. Des.*, 2011, **17**(22), 2331–2351.

59 M. T. I. S. Munaweera, *Nanoparticles and Nanofiber Composites for Drug Delivery, Cancer Chemoradiotherapy and Other Biological Applications*, The University of Texas at Dallas, 2015.

60 A. R. Bhalekar and L. N. Singh, Structural and Magnetic Studies of Aluminum Substituted YIG Nanoparticles Prepared by a Sol-Gel Route, *Braz. J. Phys.*, 2019, **49**(5), 636–645.

61 Z. Xia and A. Meijerink, Ce 3^{+}-Doped garnet phosphors: composition modification, luminescence properties and applications, *Chem. Soc. Rev.*, 2017, **46**(1), 275–299.

62 A. Jain, P. Sengar and G. A. Hirata, Rare-earth-doped $Y_3Al_5O_{12}$ (YAG) nanophosphors: synthesis, surface functionalization, and applications in thermoluminescence dosimetry and nanomedicine, *J. Phys. D: Appl. Phys.*, 2018, **51**(30), 303002.

63 A. Sunny, V. Viswanath, K. P. Surendran and M. T. Sebastian, The effect of Ga^{3+} addition on the sinterability and microwave dielectric properties of $RE_3Al_5O_{12}$ (Tb^{3+}, Y^{3+}, Er^{3+} and Yb^{3+}) garnet ceramics, *Ceram. Int.*, 2014, **40**(3), 4311–4317.

64 R. K. Singh, N. Jain, P. Singh, R. Kumar, J. Singh, S. Dutta, T. M. Chen, S. Som and H. C. Swart. Development in the innovation of lead halide-based perovskite quantum dots from rare earth-doped garnet-based phosphors for light-emitting diodes, in *Spectroscopy of Lanthanide Doped Oxide Materials*, Woodhead Publishing, 2020, pp. 21–56.

65 G. B. Scott and D. Lacklison, Magneto-optic properties and applications of bismuth substituted iron garnets, *IEEE Trans. Magn.*, 1976, **12**(4), 292–311.

66 H. B. Vasili, B. Casals, R. Cichelero, F. Macià, J. Geshev, P. Gargiani, M. Valvidares, J. Herrero-Martin, E. Pellegrin, J. Fontcuberta and G. Herranz, Direct observation of multivalent states and 4 f → 3 d charge transfer in Ce-doped yttrium iron garnet thin films, *Phys. Rev. B*, 2017, **96**(1), 014433.

67 M. C. Onbasli, L. Beran, M. Zahradník, M. Kučera, R. Antoš, J. Mistrík, G. F. Dionne, M. Veis and C. A. Ross, Optical and magneto-optical behavior of Cerium Yttrium Iron Garnet thin films at wavelengths of 200–1770 nm, *Sci. Rep.*, 2016, **6**(1), 1–10.

68 S. Higuchi, Y. Furukawa, S. Takekawa, O. Kamada, K. Kitamura and K. Uyeda, Magneto-optical properties of cerium-substituted yttrium iron garnet single crystals for magnetic-field sensor, *Sens. Actuators, A*, 2003, **105**(3), 293–296.

69 F. Chen, X. Wang, Y. Nie, Q. Li, J. Ouyang, Z. Feng, Y. Chen and V. G. Harris, Ferromagnetic resonance induced large microwave magnetodielectric effect in cerium doped $Y_3Fe_5O_{12}$ ferrites, *Sci. Rep.*, 2016, **6**(1), 1–8.

70 L. Soumah, N. Beaulieu, L. Qassym, C. Carrétéro, E. Jacquet, R. Lebourgeois, J. B. Youssef, P. Bortolotti, V. Cros and A. Anane, Ultra-low damping insulating magnetic thin films get perpendicular, *Nat. Commun.*, 2018, **9**(1), 1–6.

71 T. Goto, M. C. Onbaşlı and C. A. Ross, Magneto-optical properties of cerium substituted yttrium iron garnet films with reduced thermal budget for monolithic photonic integrated circuits, *Opt. Express*, 2012, **20**(27), 28507–28517.

72 S. Higuchi, K. Ueda, F. Yahiro, Y. Nakata, H. Uetsuhara, T. Okada and M. Maeda, Fabrications of cerium-substituted YIG thin films for magnetic field sensor by pulsed-laser deposition, *IEEE Trans. Magn.*, 2001, **37**(4), 2451–2453.

73 A. Ikesue, Y. L. Aung, R. Yasuhara and Y. Iwamoto, Giant Faraday rotation in heavily ce-doped YIG bulk ceramics, *J. Eur. Ceram. Soc.*, 2020, **40**(15), 6073–6078.

74 S. M. Elhamali, N. B. Ibrahim and S. Radiman, Influence of erbium on the structural, optical and magnetic properties of sol–gel Ce: YIG films, *J. Sol-Gel Sci. Technol.*, 2018, **85**(3), 693–702.

75 M. R. Khalifeh, H. Shokrollahi, F. S. Nogorani and M. Basavad, Improving Dy, Ce, Bi: YIG phase formation and magnetic features *via* heat treatment and chemical composition, *Appl. Phys. A: Solids Surf.*, 2020, **126**(9), 1–16.

76 M. Golkari, H. Shokrollahi and H. Yang, The influence of Eu cations on improving the magnetic properties and promoting the Ce solubility in the Eu, Ce-substituted garnet synthesized by the solid state route, *Ceram. Int.*, 2020, **46**(7), 8553–8560.

77 T. C. Mao and J. C. Chen, Influence of the addition of CeO_2 on the microstructure and the magnetic properties of yttrium iron garnet ceramic, *J. Magn. Magn. Mater.*, 2006, **302**(1), 74–81.

78 P. Pahuja, C. Prakash and R. P. Tandon, Comparative study of magnetoelectric composite system Ba0. $95Sr_{0.05}TiO_3$–$Ni_{0.8}Co_{0.2}Fe_2O_4$ with ferrite prepared by different methods, *Ceram. Int.*, 2014, **40**(4), 5731–5743.

79 G. Gurjar, V. Sharma, S. Patnaik and B. K. Kuanr, Structural and magnetic properties of high quality single crystalline YIG thin film: A comparison with the bulk YIG, *AIP Conf. Proc.*, 2019, **2115**(No. 1), 030323.

80 B. Bhoi, N. Venkataramani, R. P. R. C. Aiyar and S. Prasad, FMR and magnetic studies on polycrystalline YIG thin films deposited using pulsed laser, *IEEE Trans. Magn.*, 2013, **49**(3), 990–994.

81 V. Sharma, J. Saha, S. Patnaik and B. K. Kuanr, YIG based broad band microwave absorber: A perspective on synthesis methods, *J. Magn. Magn. Mater.*, 2017, **439**, 277–286.

82 S. Geller and M. A. Gilleo, The crystal structure and ferrimagnetism of yttrium-iron garnet, Y_3Fe_2 $(FeO_4)_3$, *J. Phys. Chem. Solids*, 1957, **3**(1–2), 30–36.

© 2021 The Author(s). Published by the Royal Society of Chemistry

Open Access Article. Published on 25 August 2021. Downloaded on 2/22/2026 9:18:43 AM.
This article is licensed under a Creative Commons Attribution-NonCommercial 3.0 Unported Licence.

83 M. Basavad, H. Shokrollahi and M. Golkari, Effect of thermal cycle and Bi/Eu doping on the solubility of Ce in YIG, *Ceram. Int.*, 2020, **46**(12), 20144–20154.

84 S. Tan, W. Zhang, L. Yang, J. Chen and Z. Wang, Intrinsic defects in yttrium iron garnet: A first-principles study, *J. Appl. Phys.*, 2020, **128**(18), 183904.

85 D. Nath, F. Singh and R. Das, X-ray diffraction analysis by Williamson-Hall, Halder-Wagner and size-strain plot methods of CdSe nanoparticles-a comparative study, *Mater. Chem. Phys.*, 2020, **239**, 122021.

86 J. Saini, D. Yadav, V. Sharma, M. Sharma and B. K. Kuanr, Effect of Aliovalent Substitution in Y 2.9 Bi 0.1 Fe_5O_{12}: Magnetization Dynamic Study, *IEEE Trans. Magn.*, 2020, **57**(2), 1–5.

87 J. J. Song, P. B. Klein, R. L. Wadsack, M. Selders, S. Mroczkowski and R. K. Chang, Raman-active phonons in aluminum, gallium, and iron garnets, *J. Opt. Soc. Am.*, 1973, **63**(9), 1135–1140.

88 E. J. J. Mallmann, A. S. B. Sombra, J. C. Goes and P. B. A. Fechine, Yttrium iron garnet: properties and applications review, *Solid State Phenom.*, 2013, **202**, 65–96.

89 R. Nazlan, I. Ismail, Z. Abbas, I. R. Ibrahim, F. M. Idris, F. N. Shafiee, A. S. Aripin and N. A. N. Busra, Dependence of magnetic and microwave loss on evolving microstructure in yttrium iron garnet, *J. Mater. Sci.: Mater. Electron.*, 2018, **29**(10), 8688–8700.

90 O. Opuchovic, M. Andrulevicius, S. Tamulevicius, J. L. Rehspringer, A. Beganskiene, R. Skaudzius, K. Ishikawa and A. Kareiva, Cerium doping and cerium aluminium co-doping effects on the sol-gel processing of $Y_3Fe_5O_{12}$ (YIG): Bulk and thin films, *Solid State Sci.*, 2020, **99**, 106065.

91 M. N. Akhtar, A. B. Sulong, M. A. Khan, M. Ahmad, G. Murtaza, M. R. Raza, R. Raza, M. Saleem and M. Kashif, Structural and magnetic properties of yttrium iron garnet (YIG) and yttrium aluminum iron garnet (YAIG) nanoferrites prepared by microemulsion method, *J. Magn. Magn. Mater.*, 2016, **401**, 425–431.

92 R. B. Borade, S. E. Shirsath, G. Vats, A. S. Gaikwad, S. M. Patange, S. B. Kadam, R. H. Kadam and A. B. Kadam, Polycrystalline to preferred-(100) single crystal texture phase transformation of yttrium iron garnet nanoparticles, *Nanoscale Adv.*, 2019, **1**(1), 403–413.

93 M. Niyaifar and H. Mohammadpour, Study on magnetic role of Bi3+ ion by random cation distribution model in Bi–YIG system, *J. Magn. Magn. Mater.*, 2015, **396**, 65–70.

94 M. Niyaifar and H. Mohammadpour, Study on magnetic role of Bi3+ ion by random cation distribution model in Bi–YIG system, *J. Magn. Magn. Mater.*, 2015, **396**, 65–70.

95 Z. Cheng, Y. Cui, H. Yang and Y. Chen, Effect of lanthanum ions on magnetic properties of Y 3 Fe 5 O 12 nanoparticles, *J. Nanopart. Res.*, 2009, **11**(5), 1185–1192.

96 Z. Cheng, H. Yang, L. Yu and W. Xu, Saturation magnetic properties of Y_{3-x} $Re_xFe_5O_{12}$ (Re: Gd, Dy, Nd, Sm and La) nanoparticles grown by a sol–gel method, *J. Mater. Sci.: Mater. Electron.*, 2008, **19**(5), 442–447.

97 G. F. Dionne, *Magnetic Oxides*, New York, Springer, 2009, vol. 14, p. 15.

98 H. Kirchmayr, *Magnetic Anisotropy*, 2001.

99 D. Polder, VIII. On the theory of ferromagnetic resonance, *London Edinburgh Philos. Mag. J. Sci.*, 1949, **40**(300), 99–115.

100 J. H. Van Vleck, Concerning the theory of ferromagnetic resonance absorption, *Phys. Rev.*, 1950, **78**(3), 266.

101 K. Seemann, H. Leiste and C. Klever, Determination of intrinsic FMR line broadening in ferromagnetic (Fe44Co56) 77Hf12N11 nanocomposite films, *J. Magn. Magn. Mater.*, 2010, **322**(20), 2979–2983.

102 L. Qiao, X. Han, B. Gao, J. Wang, F. Wen and F. Li, Microwave absorption properties of the hierarchically branched Ni nanowire composites, *J. Appl. Phys.*, 2009, **105**(5), 053911.

103 B. Heinrich, J. F. Cochran and R. Hasegawa, FMR line broadening in metals due to two-magnon scattering, *J. Appl. Phys.*, 1985, **57**(8), 3690–3692.

104 Y. P. Fu, C. W. Cheng, D. S. Hung and Y. D. Yao, Formation enthalpy and magnetic properties of Bi-YIG powders, *Ceram. Int.*, 2009, **35**(4), 1509–1512.

105 Y. J. Siao, X. Qi, C. R. Lin and J. C. A. Huang, Dielectric relaxation and magnetic behavior of bismuth-substituted yttrium iron garnet, *J. Appl. Phys.*, 2011, **109**(7), 07A508.

106 H. Xu, H. Yang, W. Xu and L. Yu, Magnetic properties of Bi-doped $Y_3Fe_5O_{12}$ nanoparticles, *Curr. Appl. Phys.*, 2008, **8**(1), 1–5.

107 M. Golkari, H. Shokrollahi and H. Yang, The influence of Eu cations on improving the magnetic properties and promoting the Ce solubility in the Eu, Ce-substituted garnet synthesized by the solid state route, *Ceram. Int.*, 2020, **46**(7), 8553–8560.

108 E. Baños-López, C. A. Cortés-Escobedo, F. Sánchez-De Jesús, A. Barba-Pingarrón and A. M. Bolarín-Miró, Crystal structure and magnetic properties of cerium-doped YIG: Effect of doping concentration and annealing temperature, *J. Alloys Compd.*, 2018, **730**, 127–134.

© 2021 The Author(s). Published by the Royal Society of Chemistry